ACS NANO

www.acsnano.org

ARTICLE

Intelligent Olfactory System Utilizing *In Situ* Ceria Nanoparticle-Integrated Laser-Induced Graphene

Hyeongtae Lim, Hyeokjin Kwon, Jae Eun Jang, and Hyuk-Jun Kwon*

Cite This: *ACS Nano* 2025, 19, 17850–17862

Read Online

ACCESS | Metrics & More | Article Recommendations | Supporting Information

ABSTRACT: **The digitization of human senses has driven innovation across various technologies and transformed our daily lives, yet the digitization of olfaction remains a challenging frontier. Artificial olfactory systems, or electronic noses (e-noses), offer great potential for environmental monitoring, food safety, healthcare, and the fragrance industry. However, integrating sensor arrays that mimic olfactory receptors remains difficult, typically requiring complex, repetitive, and costly fabrication processes. In this research, we report the development of a porous laser-induced graphene (LIG) sensor array with *in situ*-doped cerium oxide nanoparticles for the classification of odorant molecules. By adjusting the laser irradiation parameters, we achieve a high degree of physical and chemical diversity in both LIG and CeO_x. Consequently, a sensor array exhibiting diverse response patterns to different odorant molecules can be fabricated through one-step laser irradiation of a polymer precursor. Using *t*-distributed stochastic neighbor embedding (*t*-SNE) and support vector machine (SVM)-based machine learning, we accurately predict the type and concentration of nine odorant molecules used in perfumes and cosmetics, achieving a high accuracy exceeding 95%. This study provides a rapid and straightforward solution for creating functional olfactory receptor-mimicking arrays, advancing the development of artificial olfaction systems.**

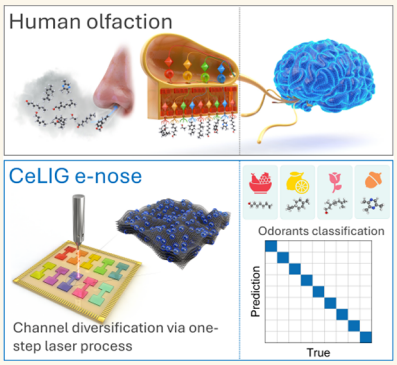

KEYWORDS: *laser-induced graphene, laser process, cerium oxide, electrical nose, odorants, machine learning, flexible device*

Human senses are increasingly digitized through sensors, which have become ubiquitous in our daily routines. Prominent examples include image sensors and displays for vision, microphones and speakers for hearing, and pressure sensors combined with haptic technology for touch. These technologies not only replicate but also extend beyond natural human capabilities, enabling the visualization of infrared light and the detection of ultrasonic sounds.[1] Notably, the olfactory process, which transmits stimuli from gaseous chemical substances to the olfactory cortex via electrical signals, plays a crucial role in detecting hazardous smells for survival and has vast potential applications in food, fragrance, and health industries. However, the digitization of the sense of smell, considered the most primal and strongly linked to human memory, has been relatively slower compared to other senses.

Odorant receptors do not bind to odorant molecules in a one-to-one manner. Instead, they use a "combinatorial coding" process, where odorant molecules bind to multiple odorant receptors to convey information about the scent (Figure 1a).[2] This mechanism allows humans to distinguish approximately one trillion different smells with only about 400 types of olfactory receptors.[3] Recent studies have attempted to mimic this olfactory system by constructing gas sensor arrays integrated with signal processing to create an electrical nose (e-nose). In the early stage, e-noses were composed of large and individual sensors, making it challenging to emulate the diversity of olfactory receptors.[4−6] Additionally, the difficulty of miniaturization limited their suitability for personalized systems and real-world applications.[7,8] To address these challenges, various methods have been explored to fabricate sensor arrays with diverse sensing materials, such as metal oxides and graphene derivatives, on an integrated single substrate.[9,10] Several groups, including Moon et al. and Kang et al., fabricated chemiresistive sensor arrays by depositing multiple metal oxides onto a 4-in. wafer to detect NO_2 and harmful VOCs, respectively.[11,12] Recent studies have also introduced catalysts and gas-active materials to improve selectivity.[13,14] However, most previous methods require

Received: February 27, 2025
Revised: April 11, 2025
Accepted: April 14, 2025
Published: April 21, 2025

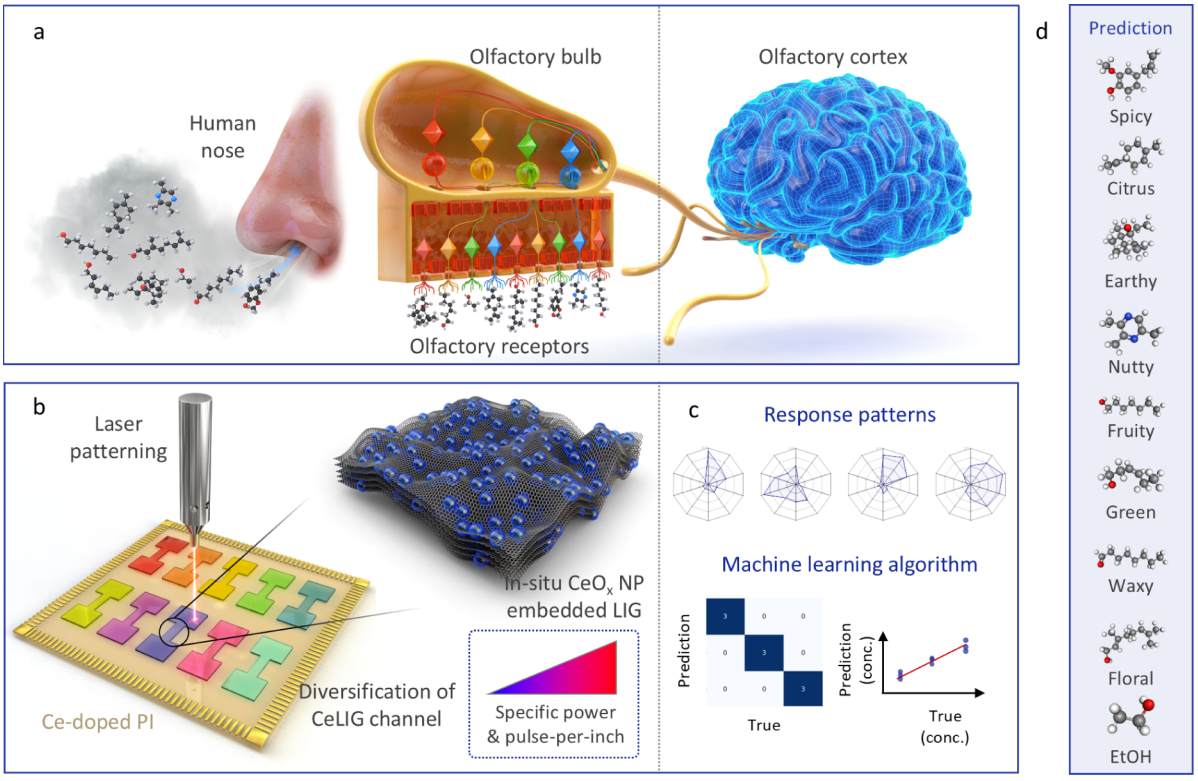

Figure 1. (a) Human olfactory olfactory system consisting of olfactory receptors, olfactory bulb, and olfactory cortex. (b) The fabrication process of the cerium oxide-doped laser-induced graphene (CeLIG) array for the facile mimicry of olfactory receptors. (c) Distinguishable response patterns and machine learning process for odorant prediction. (d) Prediction of nine odorant molecules.

complex vacuum deposition involving multiple masks to comprise diverse sensing materials. Furthermore, thin films based on chemical vapor deposition and physical vapor deposition tend to exhibit lower sensing performance due to their low surface area-to-volume ratios.[10,12,15] Meanwhile, many e-noses using graphene derivatives involve the cumbersome transfer of dispersed solutions, making them unsuitable for mass production.[16−18] Therefore, an efficient olfactory mimicking system requires the development of sensor arrays that (1) exhibit different response patterns to odorant molecules, (2) can be manufactured with simple processes, and (3) possess high surface areas.

In this article, we report a laser-induced graphene (LIG) array with uniformly *in situ* doped catalytic nanoparticles for odorant classification. LIG, obtained through direct laser irradiation of various organic or polymer substrates, has garnered remarkable attention as a chemical sensing platform due to its intrinsic porosity and abundant surface functional groups.[19−21] Although the use of pristine LIG alone is limited in gas sensor applications due to insufficient reactivity, recent studies, including our latest research, have demonstrated the real-time ultrasensitive detection capabilities of LIG integrated with functional gas sensing materials such as MoS_2, VO_2, and Cu_3HHTP_2 metal−organic frameworks (MOFs).[22−24] Furthermore, the morphological and chemical environments of LIG can be significantly altered by adjusting laser irradiation conditions. For example, varying the pulses per inch (PPI) and laser power can modify the properties of LIG, ranging from superhydrophobic to superhydrophilic, transforming its structure from isotropic pores to nanofibers or altering the number of defects.[19,25−27] Despite these impressive gas sensing performances and various tunability, previous studies have primarily applied LIG as single sensors for detecting limited specific gases (e.g., NH_3, NO_2) and have rarely been employed in e-noses for classifying odorant molecules. To address this gap, we developed an artificial olfactory system by introducing catalytic CeO_x nanoparticles into a LIG array (CeLIG, Figure 1b). Recently, ceria nanoparticles have been highly regarded as effective sensitizers in chemiresistive sensing layers due to their thermochemical stability, exceptionally high redox activity, and introduction of additional active sites.[28,29] Also, an n-type semiconducting CeO_x can form heterojunctions with the p-type carbon material, resulting in sensitive electrical transduction.[30,31] The laser irradiation process allows for the formation of the sensor array in a single step under ambient environment and easily modifies the chemical properties of LIG and CeO_x, determining the response patterns to odorant molecules.

The fabricated sensor could distinguish nine odorant molecules using *t*-distributed stochastic neighbor embedding (*t*-SNE) supported visualization platforms. Moreover, we developed a support vector machine (SVM)-based machine learning (ML) model that successfully achieved over 95% accuracy in predicting the type and concentration of exposed odorant molecules (Figure 1c,d). This study extends the application of e-noses, traditionally used for detecting highly reactive inorganic gases like NO_2, NH_3 or toxic VOCs, to odorant molecules used in perfumes and the cosmetic industry.[13,32] Finally, by utilizing LIG fabricated on lightweight polymer substrates, we demonstrated the potential for application in flexible devices, overcoming the limitations of conventional e-noses, which are predominantly confined to rigid substrates.[10,11]

https://doi.org/10.1021/acsnano.5c03601
ACS Nano 2025, 19, 17850−17862

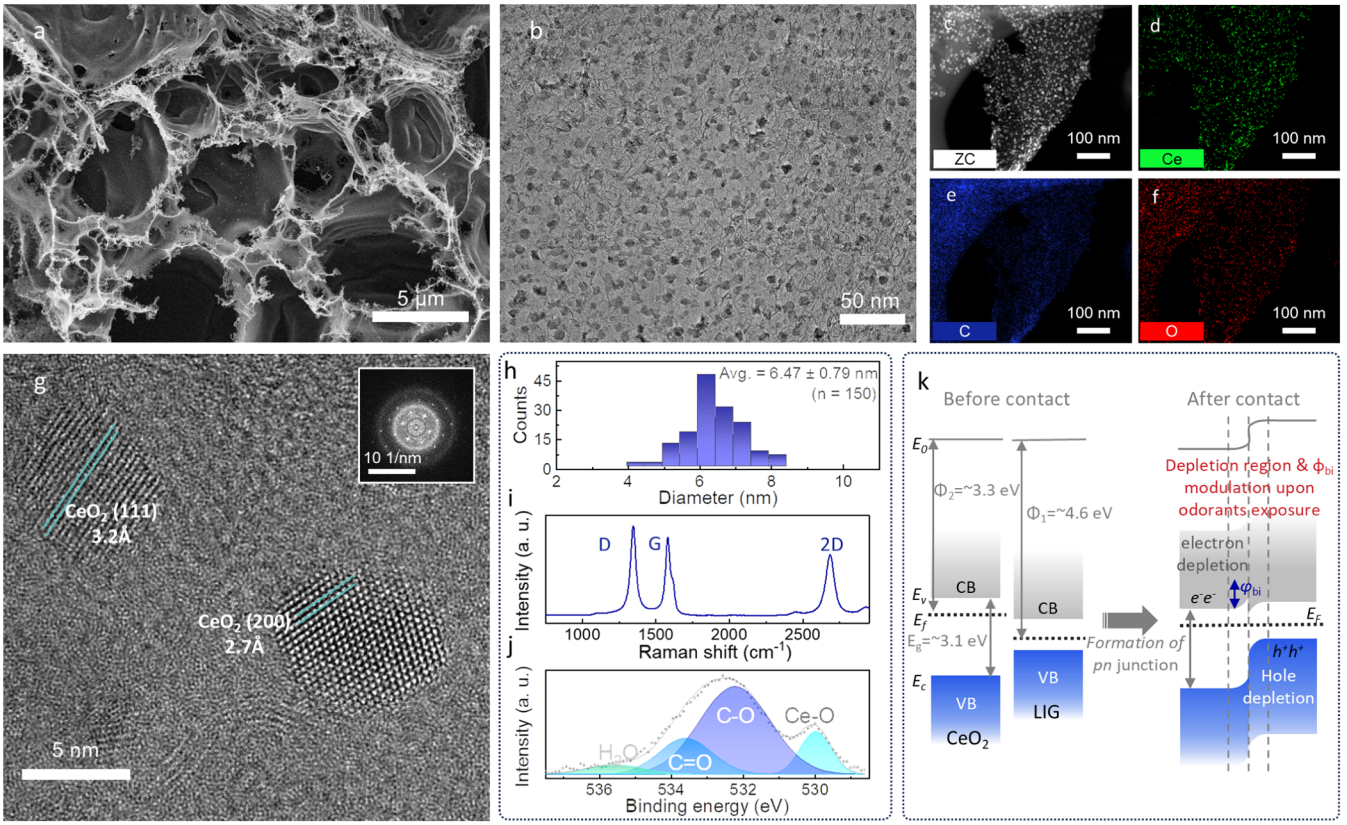

Figure 2. Analytical characterization of CeLIG. (a) The SEM image of CeLIG shows its macroporous nature. (b) The TEM image of CeLIG. (c–f) EDS-TEM images of CeLIG display a uniform distribution of all elements: electron, cerium, carbon, and oxygen maps, respectively. (g) The high-magnification TEM image of CeLIG clearly shows the CeO_2 lattice structure. (h) Uniform size distribution of cerium oxide nanoparticles embedded in LIG. (i) Raman spectrum and (j) XPS O 1s spectrum of CeLIG. (k) Energy band diagram of CeLIG illustrating the formation of the pn junction between typical cerium oxide and LIG.

RESULTS AND DISCUSSION

Fabrication of Biomimetic Olfactory Platform Using LIG. Figure 1b illustrates the fabrication process and structural schematic of CeLIG. The CeLIG platform was fabricated through direct laser irradiation of a polyimide (PI) film doped with a cerium-containing precursor. Initially, cerium nitrate was dissolved in *N*-methyl-2-pyrrolidone (NMP) solvent to facilitate direct loading into the liquid PI. This mixture was then spin-coated onto a substrate and cured at 200 °C to form a thin film. The subsequent step involved programmed laser writing under various photothermal conditions, precisely following the sensor pattern on the cerium-loaded PI film. This process enabled mask-free production of sensors, which was scalable for mass production and eliminated the need for complex vacuum equipment. During laser irradiation, the PI was converted into porous LIG, while the cerium precursor simultaneously transformed into CeO_x nanocrystals. The uniform doping of small-sized CeO_x nanoparticles is critical as it minimizes sensor-to-sensor variation and enhances the active surface area, which is essential for high-performance sensing.[33] However, the introduction of functionalities into LIG through nanoparticle coating has primarily been achieved via *ex situ* processes, such as electrodeposition and drop-casting.[21] These methods require a two-step process and often suffer from significant drawbacks, including nanoparticle aggregation, inhomogeneity (leading to device-to-device variation), and large particle sizes.[34,35] Moreover, they could alter the original morphology of LIG or collapse porosity, leading to reduced surface area.[36] To address these issues, we adopted an *in situ* fabrication process for CeLIG. This approach ensured uniform sensor fabrication, maintained the intrinsic porous structure of LIG, and significantly enhanced surface reactivity by minimizing issues related to particle aggregation and size variation. The *in situ* process also simplified production, making it more suitable for scalable manufacturing.

Analytical Characterization of Nanoparticle-Embedded LIG. We conducted a comprehensive analysis to confirm the formation of CeLIG. Please note that this section aims to confirm the formation of CeLIG processed under a representative single condition (500 PPI, 10% specific power), while the subsequent section will explore variations in channel composition due to different processing parameters. The scanning electron microscopy (SEM) image of CeLIG in Figure 2a reveals a typical interlaced porous structure of LIG. The formation of numerous macropores is attributed to local explosions and the release of gaseous species during the photothermal decomposition of the Ce-doped PI film under laser irradiation.[20] These pores are crucial for enhancing the surface area, which is beneficial for gas-sensing applications. The transmission electron microscopy (TEM) image (Figure 2b) and energy-dispersive X-ray spectroscopy (EDS) images (Figure 2c-f) show the uniform distribution of CeO_2 nanoparticles across the LIG sheet. The characteristic lattice spacings of 0.32 and 0.27 nm corresponding to the (111) and (200) planes of CeO_2, respectively, were clearly visible in high-

https://doi.org/10.1021/acsnano.5c03601
ACS Nano 2025, 19, 17850–17862

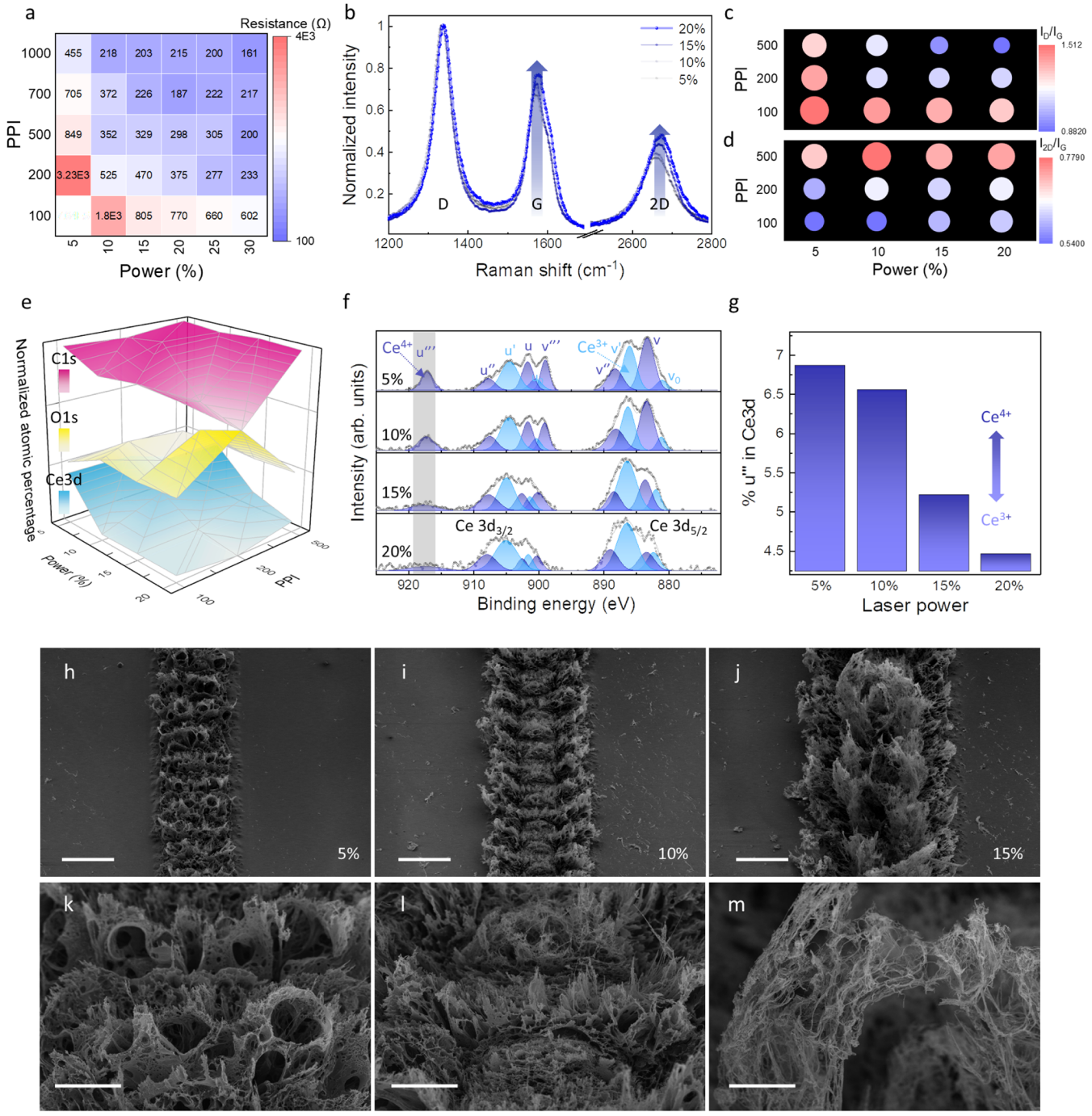

Figure 3. Chemical and physical diversification of the CeLIG sensor array. (a) Heat map of the electrical resistance regarding specific power and pulse-per-inch (PPI) of laser irradiation. (b) Raman spectra of CeLIG with different specific powers (fixed 100 PPI). (c) I_D/I_G and (d) I_{2D}/I_G ratio as a function of laser irradiation parameters. (e) Normalized atomic percentages of carbon, oxygen, and cerium with variations in specific power of laser irradiation and PPI change. (f) XPS Ce 3d spectra with increasing specific power (fixed 200 PPI). (g) Area percentages of the deconvoluted u''' peak showing the compositional changes of Ce^{3+} and Ce^{4+} with varying specific power (fixed 200 PPI). (h–m) SEM images of CeLIG processed under different specific powers in fixed 200 PPI ((h, k) 5%, (i, l) 10%, and (j, m) 15%). Scale bar, 200 μm in panels h–j and 50 μm in panels k–m.

resolution TEM (Figure 2g).[37,38] The average size of the nanoparticles was 6.47 ± 0.79 nm (Figure 2h, n = 150), with a very narrow size distribution and no signs of aggregation.

The homogeneity of CeO_2 nanoparticles was inferred from the (1) rapid heating/cooling process during nuclei formation and (2) the influence of LIG, which serves as a functional backbone. The rapid heating and cooling due to the photothermal effect of the laser could provide optimal conditions for nanoparticle synthesis. The photothermal effect induced by laser irradiation provided optimal conditions for nanoparticle synthesis, where the drastic heating ensured simultaneous formation and growth of nuclei within the irradiation area, achieving homogeneous nanoparticle size distribution.[39,40] Moreover, minimizing the movement of nanoclusters during thermal treatment was also crucial for nanoparticle growth. Hence, the introduction of a defective

https://doi.org/10.1021/acsnano.5c03601
ACS Nano 2025, 19, 17850–17862

backbone for strong surface coupling with nanoclusters has been highlighted.[37] LIG possessed an abundance of defect sites and functional groups, as indicated by a strong D peak in the Raman spectrum of graphitic material (I_D/I_G = 1.147, Figure 2i). Also, in X-ray photoelectron spectroscopy (XPS) revealing the chemical environment of CeLIG (Figure 2j), the O 1s spectrum showed a strong C−O peak (532.1 eV) and C═O peak (533.5 eV) along with O−Ce peak (529.9 eV), which indicates the presence of hydroxyl and carboxyl groups on the LIG carbon surface.[21] Therefore, the surface-functionalized LIG carbon backbone could assist in the stabilization and immobilization of cerium nanoclusters, preventing their uncontrolled coalescence. Furthermore, the *in situ*-formed CeO_2 nanoparticles, being monolithically generated, could strongly bind with the backbone compared to *ex situ* transfer methods, providing enhanced stability for applications in gas sensing, catalytic reactions, or under mechanical movements.[37,41] Thus, we successfully embedded small-sized CeO_2 nanoparticles uniformly into LIG using the laser process.

The energy band diagram of CeLIG (Figure 2k) elucidates the enhancement in gas sensing performance due to CeO_x doping. When n-type CeO_2, with a bandgap energy of 3.1 eV and a work function of 3.3 eV, forms a junction with p-type narrow bandgap LIG, which has a work function of 4.5 eV, a depletion layer is established due to the built-in potential (Figure S1).[42] This pn heterojunction at the interface is an effective strategy for enhancing the sensing performance of gas sensors based on metal oxides and various carbon derivatives.[9,22] In particular, the heterostructure with well-dispersed nanoparticles maximizes the number of depletion layers, thereby amplifying the conversion of chemical changes into electrical signals. When the adsorbed target gas is a reducing gas, the electron concentration in CeO_x increases, strengthening the pn junction, which in turn widens the depletion layer and increases resistance.[43] Conversely, when an oxidizing gas is adsorbed, the energy band shifts in the opposite direction, leading to a decreased resistance. Thus, even minor changes in charge carrier concentration can be effectively translated into significant sensor responses.

Chemical and Structural Diversification of Sensors through Laser Parameter Changes. The diversity of sensors is crucial to enhance the performance of artificial olfactory devices. A sensor array with different chemical and physical properties can generate distinguishable response patterns for various odorants, thereby improving classification accuracy. To achieve this diversity, we adjusted the specific power and PPI, which are the most commonly used parameters for tuning the chemical and physical characteristics of LIG using commercial laser sources.[19,25,44] The PPI parameter represents the pulse stacking density along the laser traveling direction.

Figure 3a shows the heat map of electrical resistance changes in response to varying laser parameters. Increased laser power and PPI elevated the laser fluence, promoting the graphitization of PI substrate and resulting in lower resistance.[44] In addition, Figure 3b−d displays the results of Raman spectroscopy, a powerful tool for characterizing carbon derivatives. The appearance of the G and D peaks confirmed the conversion of the polymer precursor into sp^2 carbon-rich materials.[45] Also, the presence of the 2D peak, which is the second-order overtone of the D peak, served as a fingerprint for graphitic material.[46] As the specific power increased from 5% to 20% and the PPI increased from 100 to 500, the I_D/I_G ratio, which signifies the defect density, decreased from a maximum of 1.51 to a minimum of 0.88. Conversely, the I_{2D}/I_G ratio, indicating thinner sp^2 carbon layers and the quality of graphene, increased from a minimum of 0.54 to a maximum of 0.77. The increased laser fluence induced localized high temperature and pressure conditions, which enhanced the carbonization, graphitization and exfoliations, thereby producing thinner and higher quality sp^2 carbon layers.[19,20] This trend is consistent with resistance heatmap results (Figure 3a). Although LIG-based e-nose systems have not been reported, previous studies using reduced graphene oxide (rGO) achieved gas selectivity by varying the reducing agents, leading to different quantities of defects and functional groups.[16] Therefore, this study presents a method to create various sensors with different reaction characteristics depending on the degree of graphene exfoliation, surface oxidation, and defect density by changing laser irradiation conditions without complicated wet chemistry.

Figure 3e displays the three-dimensional mapping of the atomic percentages of carbon, oxygen, and cerium, calculated using XPS surface analysis. Each element was normalized for visualization. Also, the ratios of oxygen and cerium atoms to carbon atoms and the original data are provided in Figure S2 and Tables S1−S3, respectively. Laser irradiation under ambient conditions led to the oxidation of the carbon surface as the specific power increased.[20] Consequently, the carbon content decreases while the oxygen content increases. This change was most pronounced under the 200 PPI condition. Additionally, the atomic percentage of cerium varied from 0.19% to 0.89%, depending on the laser parameters.

The variation in laser parameters not only affected the carbon backbone of CeLIG but also introduced diversity in the CeO_x nanoparticles. The chemical environment and valence state of CeO_x catalytic nanoparticles in CeLIG were investigated through the XPS Ce 3d scan, as shown in Figure 3f. The oxidation state of cerium significantly affects the energy structure, bandgap, and redox catalytic activity, thereby diversifying gas response patterns.[42] Specifically, many studies have demonstrated that the amount of Ce^{3+} significantly and directly enhances the catalytic activity of cerium oxide.[29,37,47,48] The Ce 3d core-level spectrum was divided into the ″u″ and ″v″ groups, corresponding to Ce 3d3/2 and Ce 3d5/2, respectively, with a spin−orbit separation of 18.6 eV. Each component was further split into multiple peaks. Peaks at v (882.8 eV), v″ (887.8 eV), v‴ (898.6 eV), u (901.4 eV), u″ (907.4 eV), and u‴ (916.9 eV) were attributed to Ce^{4+} states, while peaks v_0 (880.5 eV), v′ (885.4 eV), u_0 (900.1 eV), and u′ (904.2 eV) indicated Ce^{3+} states. This observation suggested the coexistence of Ce (III) and Ce (IV) mixed valency state within CeO_x, implying high redox activity of Ce. Notably, the quantification of Ce^{3+} was implemented by calculating the relative percentage area of the u‴ peak, which is unrelated to the amount of Ce^{3+} (i.e., the area of the u‴ peak is inversely correlated to the amount of Ce^{3+}).[47,49] Thus, it was observed that the proportion of Ce^{3+} increased with rising laser power (Figure 3g). This phenomenon is attributed to the increased power of the laser process, which promotes the generation of oxygen vacancies in the metal oxide at high temperatures, thereby encouraging the formation of Ce^{3+} to maintain charge neutrality.[29,50,51] Therefore, varying the laser parameters could create a gradient in the amount of Ce^{3+} and consequently modulate the catalytic activity of cerium oxide. Furthermore, as the amount of Ce^{3+} increases, Ce 4f orbitals become partially filled, narrowing the bandgap and resulting in changes in the

https://doi.org/10.1021/acsnano.5c03601
ACS Nano 2025, 19, 17850−17862

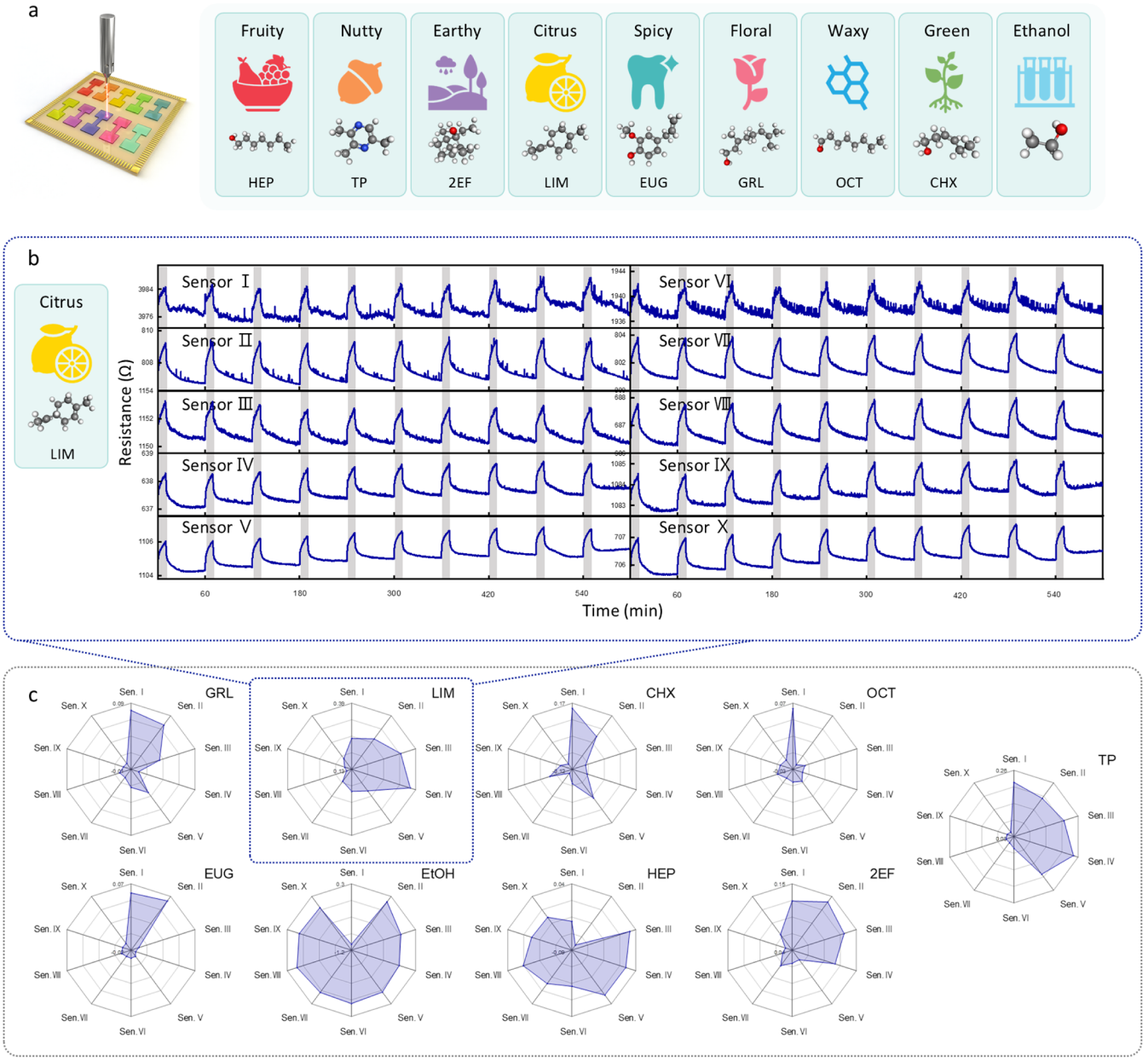

Figure 4. CeLIG response data for different odorants. (a) Structural formulas of nine odorant molecules used in the fragrance industry (1-heptanol, 2,3,5-trimethylpyrazine, 2-ethylfenchol, D-limonene, eugenol, geraniol, octanal, cis-3-hexenol, and ethanol). (b) Dynamic sensing curve for ten CeLIG sensors for D-limonene at 1000 sccm gas flow (10 min for exposure and 50 min for recovery). (c) Polar plots showing diverse response patterns of ten sensors to different odorants. All measurements were conducted at room temperature without using a heater.

depletion region, as shown in Figure 2k.[29,52] These changes lead to a diversification of gas response patterns, providing a straightforward method for designing sensor arrays.

The laser process could also impart morphological diversity to LIG. As shown in SEM images (Figure 3h–m), as specific power increased, the formation of the large volume of anisotropic fibers became more pronounced, whereas lower power conditions yielded isotropic porous structures. The rapid generation of gas due to laser irradiation drastically increased the local pressure, causing simultaneous carbonization, expansion, and exfoliation, which can transition the LIG from a porous to a fiber-like structure.[19,26]

Odorants Classification with CeLIG-Based E-Nose. Leveraging the chemical and physical diversity introduced into CeLIG through variations in laser parameters (specific power and PPI), we developed an artificial olfactory sensor array. This array consisted of ten sensors, each fabricated under different laser irradiation conditions (details provided in the Methods section). The sensor array was tested against nine representative odorants with cognitive significance—geraniol (floral), D-limonene (citrus), octanal (waxy), eugenol (spicy), 1-heptanol (fruity), 2-ethylfenchol (earthy), cis-3-hexenol (green), 2,3,5-trimethylpyrazine (nutty)—and ethanol, as shown in Figure 4a. These scents are nontoxic and possess unique aromas, making them widely used in fragrances, food additives, and perfumes.[53] As illustrated in Figure 4b, repeated exposure to these scents resulted in changes in the resistance values of each sensor, from which the response value was calculated. Thus, we

https://doi.org/10.1021/acsnano.5c03601
ACS Nano 2025, 19, 17850–17862

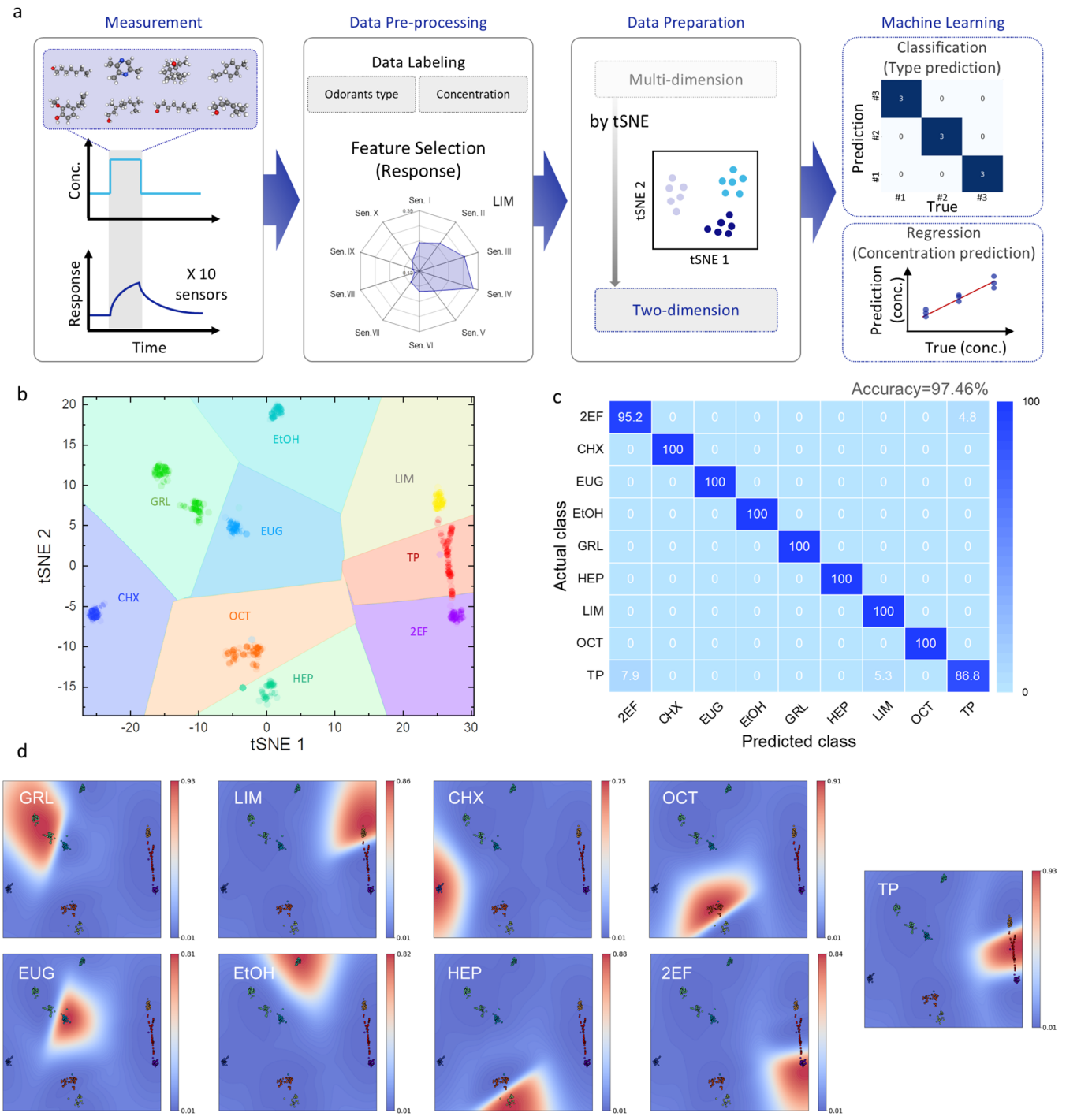

Figure 5. Odorant classification using machine learning algorithms. (a) Schematic illustrations of the data processing strategy for machine learning-based odorant prediction. (b) Classification results of nine different odorant molecules by t-SNE and SVM algorithms. (c) Confusion matrix of the actual versus predicted classes in the training set. (d) Uncertainty estimates in the form of predicting probabilities (the axis range is identical to that of Figure 5b).

could extract ten features for each scent from the sensor array. The average response values were plotted on a radar graph, as shown in Figure 4c (the overall measured response values in each sensor are provided in Tables S4−S12). As a result, it was possible to confirm distinct response patterns that allow clear differentiation between the scents. Additionally, unlike traditional metal oxide semiconductor gas sensors that typically require high temperatures (>250 °C) or light sources for activation, the LIG-based gas sensor can operate at room temperature, which makes it energy-efficient, simplifies the device configuration, and enables the use of flexible substrates.[9,22,23]

It is important to note that odorant molecules often possess multiple functional groups or complex structures. For example, these molecules comprise various combinations of different length alkyl groups (methyl, ethyl, heptyl, etc.), which act as nearly nonpolar electron donors, alcohol groups as strong electron donors, phenol and ether groups as weak donors,

https://doi.org/10.1021/acsnano.5c03601
ACS Nano 2025, 19, 17850−17862

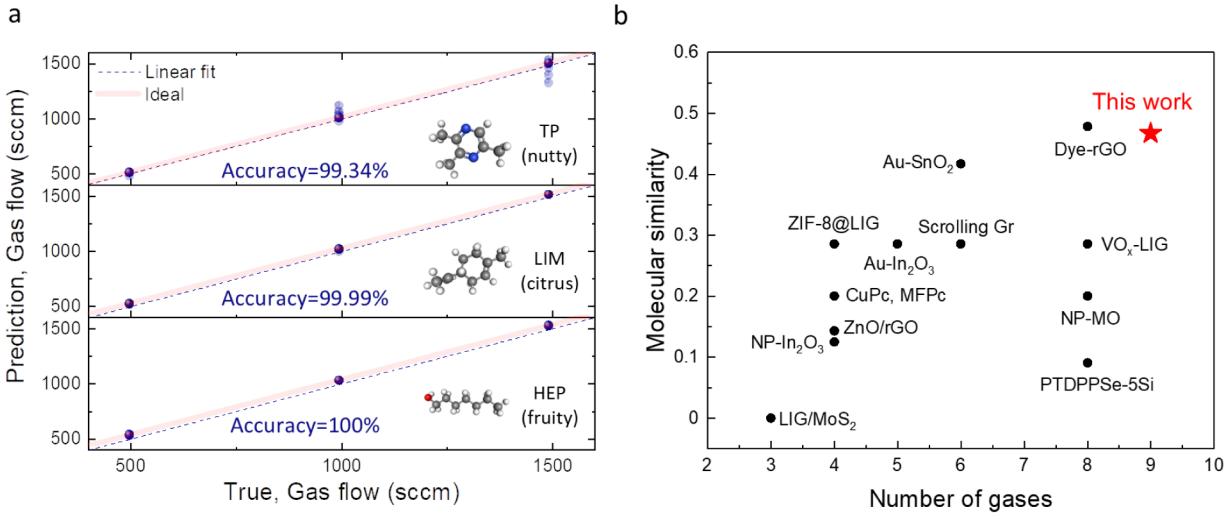

Figure 6. Machine learning-based odorant prediction data and performance comparison. (a) Predicted odorant concentration versus true odorant concentration for 2,3,5-trimethylpyrazine, D-limonene, and 1-heptanol in the training set. (b) Comparison of reported room-temperature chemiresistive gas sensors in terms of the number of gases and molecular similarity (Tanimoto coefficient).

aldehydes as weak acceptors, and pyrazine rings as intermediate acceptors. Consequently, these molecules have rarely been used in previous gas sensor studies to avoid complexity, and their reaction mechanisms remain largely unexplored. In practical applications for diverse odor molecule classification, a one-to-one match of reaction mechanisms with gas sensor arrays may be inefficient. Therefore, this study emphasizes the development of sensors capable of generating significant differences in response patterns rather than focusing on one-to-one reaction mechanisms between sensors and odor molecules.

Figure 5a illustrates the data processing workflow for predicting the types and concentrations of odorant molecules using ML. First, as shown in Figure 4, the responses of ten integrated sensors were collected for various types and conditions of gas species. The classes and concentrations of odorant molecules were then labeled in the data set. For ML feature data, the response values from the ten sensors were extracted and subjected to dimensionality reduction using *t*-SNE, transforming the data into a 2D space. This unsupervised learning-based data preparation allows high-dimensional data with many features to be represented in a reduced-dimensional space while preserving the distances between data points, thus aiding in computational efficiency and visualization.[10,54,55] Finally, the labeled data (answer data) and feature data were used to train the SVM algorithm, one of the most popular and powerful supervised learning algorithms. The trained model was utilized to classify the type of odorants and predict their concentrations through regression.

The scatter plot of Figure 5b presents the *t*-SNE results derived from the response values obtained from the CeLIG-integrated sensor array. The *t*-SNE algorithm identified a 2D representation that best preserves the distances between data points.[54] Through manifold learning, the 10-dimensional Euclidean distances were converted to 2D coordinates, allowing each odorant molecule class to be distinctly clustered without overlap. This approach provided a meaningful visualization of the large data set, which was too complex to analyze in its original form (Tables S4−S12) or via the radial plot (Figure 4c).

In order to identify and predict nine different ordered molecules, ML was performed using the obtained *t*-SNE data as feature data. SVM, a widely used supervised learning technique for classification problems, is an algorithm that finds a hyperplane to classify data and can learn an effective classifier in the feature space using the kernel method.[7,10] In this study, the SVM model was implemented with a radial basis function kernel to enhance its ability to handle nonlinear relationships within the data. The data set was split into 70% for training and 30% for testing, with the SVM model trained on the training set and its performance evaluated on the test set. For accurate generalization, the test set was not used for parameter selection or model training. Figure 5b shows the results of applying the SVM model to display the decision boundary map of 2D *t*-SNE coordinates. The trained model provided distinguishable boundaries for the nine odorants within the dimensionally reduced space, offering clear visual information. Figures 5c and S3 show the confusion matrix of the actual versus predicted classes for the nine odorants from the trained SVM classification results. The trained model demonstrated a high prediction accuracy of 97.46% on the training set and 97.06% on the test set, indicating successful generalization without overfitting or underfitting. Figure 5d illustrates the uncertainty estimates from the classifier in the form of predicting probabilities. Each subplot corresponds to a specific odorant class, with the color gradients on the heatmap depicting the model's confidence in predicting each class. Red regions on the map indicate high probabilities, suggesting that the classifier is highly confident in those predictions, while blue regions represent lower probabilities, indicating areas of uncertainty or weaker classification confidence. Therefore, the trained classifier shows concentrated high-probability regions that do not significantly overlap, resulting in a low risk of false positives or false negatives.

The concentration of odorants was predicted by utilizing support vector regression from the scikit-learn machine-learning library. The concentration of fragrance plays a key role in determining the depth, persistence, and overall perception of the fragrance. As the ratio of carrier gas to base gas increases to 1:3, 1:1, and 3:1, Figures 6a and S4 show the true concentration data on the *x*-axis and the predicted

https://doi.org/10.1021/acsnano.5c03601
ACS Nano 2025, 19, 17850−17862

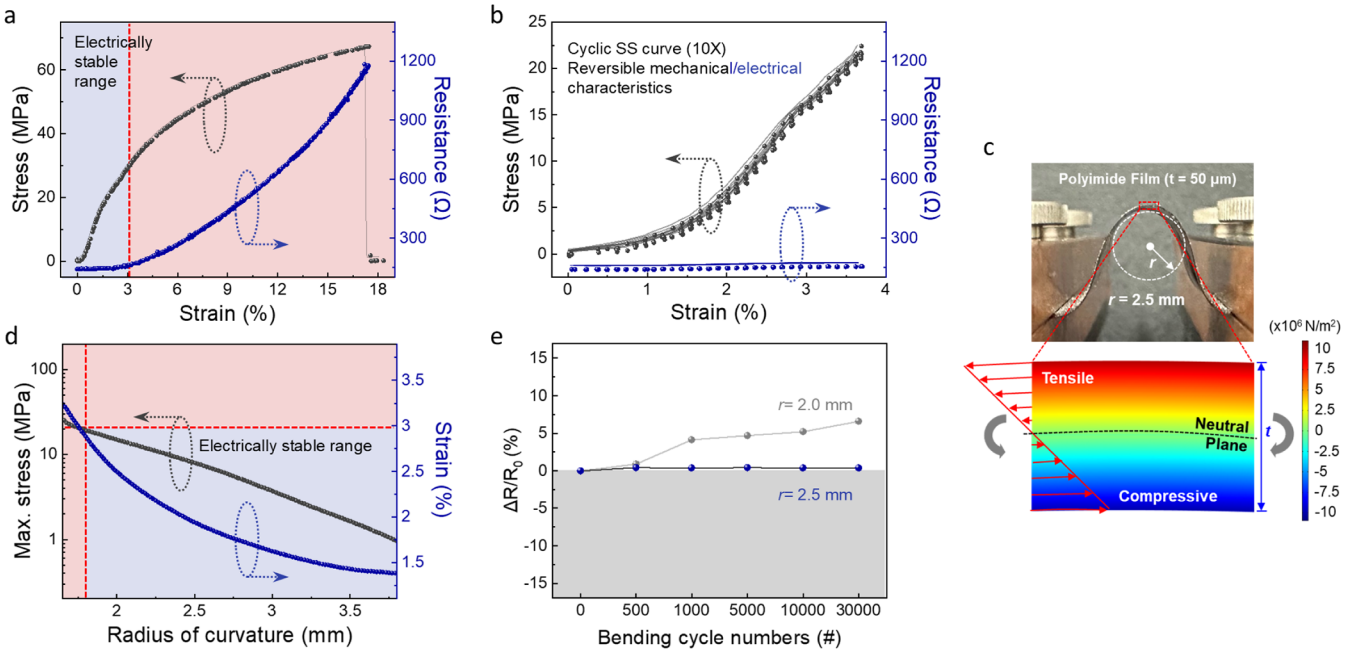

Figure 7. Stress analysis and flexibility test of CeLIG. (a) Stress−strain curve in a tensile process to fracture point. (b) Cyclic stress−strain curve of CeLIG on the flexible polymer substrate. (c) Computational simulation of the stress distribution of the polymer film by finite element analysis (FEA). (d) Predicted stress and strain curves regarding various bending radii. (e) The fatigue test shows no variation in electrical resistance during the cyclic bending (thickness and radius of curvature are 50 μm and 2.5 mm, respectively).

data on the *y*-axis. The solid red lines represent the ideal prediction curve ($y = x$), and the dashed blue lines show the linear approximation of the predicted data using regression. The R^2 accuracy calculated using the residual variance for the test set also showed high values, with 96.34%, 94.44%, and 99.92% for 2,3,5-trimethylpyrazine, D-limonene, and 1-heptanol, respectively (99.34%, 99.99%, and 100% for the training set). These results demonstrate that *t*-SNE-based data processing provides clear and intuitive visual information, and ML-based models can accurately predict both the type and concentration of odorants.

Odors in real-world environments often exist as complex mixtures rather than single compounds, as seen in multicomponent perfumes. Identifying individual components within such mixtures is crucial for developing practical sensors. To address this, we adopted multivariate SVM regression to predict the concentrations of individual molecules within a mixture. Figure S5 illustrates the results of predicting the concentrations of d-limonene, which has a fresh citrus aroma, and eugenol, known for its distinctive spicy scent, in their mixture. Our olfactory system successfully predicted the concentrations of each component with an accuracy of over 98% on both the training and test data sets. Similarly, in the mixture of cis-3-hexenol (green) and geraniol (floral), the concentrations of individual elements could be predicted with high accuracies of 98.3% and 94.47% for the training and test sets, respectively (Figure S6). These results demonstrate the system's ability to accurately estimate individual components in complex mixtures, highlighting its potential to contribute to the development of next-generation electronic noses capable of distinguishing intricate odors.

To quantitatively evaluate the selectivity of the fabricated sensor, we compared it with previously reported chemiresistive type gas sensors operating at room temperature. Among the various calculation methods, the Tanimoto coefficient was selected to measure molecular similarity, which is widely utilized in cheminformatics and computational chemistry due to its computational efficiency.[56,57] Figure S7 presents a heatmap showing the similarity between each pair of odorants. Subsequently, Figure 6b displays the number of gas classes used in the selectivity assessment of reported room-temperature chemiresistive type gas sensors and their molecular similarity, including our study.[22,58−69] The molecular similarity used here was the maximum value derived from calculating the Tanimoto coefficient for all possible gas pairs. The results indicated that the fabricated CeLIG sensor array could effectively distinguish multiple types of similar gases (odors), ranking it as one of the most selective sensors.

It is important to note that this comparison includes not only e-noses designed for odor differentiation but also single sensors targeting specific gases. Artificial olfaction platforms capable of distinguishing a large number of odorant molecules at room temperature have been relatively rare. This capability, combined with the simplicity of the structure, low energy consumption, and stability, could facilitate the expansion of artificial olfaction platforms into broader applications beyond traditional targets like NO_2, NH_3, and certain VOCs to include more complex odorant molecules.

Application to a Flexible Device. Flexibility is a crucial characteristic for applying sensor platforms in various fields, such as patch-type sensors, smart packaging, or outdoor environments.[70] When designing this sensor platform, even if it has excellent mechanical stability, unstable electrical characteristics can disrupt sensor operation. To ensure reliable performance, it is crucial to establish an operating range where both mechanical and electrical stability are maintained. As shown in Figure 7a, which measures the mechanical stress and electrical resistance changes under the tensile process, the operating range should be confined within a strain of 3% (indicated by the blue-shaded area), where both mechanical

https://doi.org/10.1021/acsnano.5c03601
ACS Nano 2025, 19, 17850−17862

and electrical stability are guaranteed. Additionally, in the case of the hyperelastic flexible substrate used in this study, when a load lower than the previously applied maximum load is applied, it exhibited nonlinear and irreversible elastic behavior due to stress softening, known as the Mullins effect.[71] To more accurately predict and analyze mechanical behavior, it was necessary to conduct cyclic tests of loading and unloading within specific strain ranges to observe material behavior and take this into account. To this end, we measured the cyclic stress−strain (SS) characteristics within the strain range of 3% set earlier, as shown in Figures 7b and S8. We then applied the conditions and results that minimized changes in the SS characteristics to the mechanical behavior analysis, aiming for more accurate predictions.

Using the FEA analysis results based on the data from Figure 7b, we visualized the spatial distribution of internal stress during bending and identified the locations where maximum stress occurs (Figure 7c). This analysis allowed us to predict the minimum achievable radius of curvature, as shown in Figure 7d. We would like to note that the maximum stress and maximum strain occurred on the outermost surface of the flexible structure, where bending occurs at the smallest radius of curvature during the bending. In Figure 7d, the flexible structure could be designed to operate within a deformation range that was electrically and mechanically stable (blue-shaded area, radius of curvature > 1.7 mm).

However, the results obtained from this FEA analysis did not account for fatigue failure that may initiate from invisible microcracks as cyclic loading progresses. Thus, direct verification through cyclic loading tests was necessary. Based on the FEA results that incorporate the Mullins effect, we selected small radius curvatures of 2.0 mm and 2.5 mm, which fall within the electrically and mechanically stable range, to conduct fatigue tests (Figure 7e). Although the 2.0 mm radius of curvature was within the stable range, cyclic fatigue tests revealed that, while the structure maintained operational stability during a limited number of bending cycles, invisible damage accumulated and propagated after exceeding 1000 cycles, compromising structural stability. Conversely, at the 2.5 mm radius of curvature, which provides a safer margin within the electrically stable range, the initial resistance value was preserved even after 30,000 cycles of cyclic bending. This result indicates that flexibility optimization enables the device to operate reliably without fatigue failure under repetitive bending conditions. Therefore, the CeLIG platform holds significant potential for future applications requiring a flexible e-nose.

CONCLUSION

In this study, we demonstrated the fabrication and application of a LIG-based e-nose integrated with uniformly *in situ*-doped CeO_x nanoparticles for effective odorant classification. The *in situ* doping of CeO_x nanoparticles was achieved simultaneously with the formation of LIG through a one-step laser irradiation process, which significantly simplified the fabrication process and ensured uniform nanoparticle distribution. Notably, the laser parameters could be adjusted to fine-tune the properties of the active channels without the need for complex deposition processes, offering a convenient method for creating sensor arrays that mimic the human olfactory system. Our results showed that the CeLIG e-nose effectively classified nine distinct odorant molecules used in the cosmetics and perfume industry. The *t*-SNE technique facilitated the visualization and dimensionality reduction of the sensor data, highlighting the distinct response patterns of each odorant. Furthermore, the SVM-based ML model achieved over 95% accuracy in predicting the type and concentration of the odorants. The mechanical flexibility of the CeLIG sensors was also validated, indicating their potential for integration into flexible electronic devices and compatibility with scalable processes such as roll-to-roll printing. Collectively, this study represents a significant advancement in the development of e-noses, demonstrating their potential for applications in traditional industries like environmental monitoring, food safety, and healthcare, as well as emerging fields such as fragrance marketing. The unique combination of simplified fabrication, tunable properties, and robust classification capability positions establishes the CeLIG e-nose as a promising tool for future sensor technologies.

EXPERIMENTAL SECTION

Preparation of Precursor Materials. All chemicals were obtained from commercial sources and used without further purification. $Ce(NO_3)_3{\cdot}6H_2O$, NMP solvent, and all odorants were purchased from Sigma-Aldrich. PI liquid (VTEC PI-1388) and Kapton PI were purchased from the RBI and 3 M companies, respectively.

Fabrication of CeO_x Nanoparticle-Embedded LIG. 720 mg of $Ce(NO_3)_3{\cdot}6H_2O$ was dissolved in 8.3 mL of NMP by sonication. This solution was then mixed with 41.7 mL of liquid PI and vigorously stirred at room temperature to form a total of 50 mL of PI resin containing the cerium precursor. The solution was spin-coated onto a glass substrate covered with Kapton tape at 2000 rpm for 30 s, followed by soft baking at 100 °C. This process was repeated five times to achieve the desired thickness, and the final curing was performed at 200 °C.

The laser process for fabricating CeLIG was carried out using a Universal Laser System VLS 4.60, adjusting specific power and PPI (with speed fixed at 50%). In this process, a 25W laser cartridge was used, and the focus was adjusted to the surface of the substrate. Unless otherwise specified, the conditions used for characterizing were 10% specific power and 500 PPI. Vector scanning was used to pattern filament-type channels of 1 mm in length for the manufacturing of the sensors used for the CeLIG e-nose. The contact pad was patterned by rastering and coated with Ag paste for a stable connection with the probe tip. A total of 10 different CeLIG channels were produced under varying laser process parameters (Ch.1:5% specific power and 200 PPI, Ch.2:5% specific power and 500 PPI, Ch.3:10% specific power and 200 PPI, Ch.4:10% specific power and 500 PPI, Ch.5:15% specific power and 100 PPI, Ch.6:15% specific power and 200 PPI, Ch.7:15% specific power and 500 PPI, Ch.8:20% specific power and 100 PPI, Ch.9:20% specific power and 200 PPI, and Ch.10:20% specific power and 500 PPI).

Analytical Characterization. The morphologies of CeLIG were observed by field emission scanning electron microscopy (FE-SEM, Hitachi SU8020). The ultrahigh resolution TEM was performed using a Thermo Fisher Themis Z TEM instrument. For the preparation of TEM samples, CeLIG was peeled off from the substrate and transferred onto a lacey carbon-supported nickel TEM grid. High-resolution Raman spectra were obtained by employing a Renishaw inVia Qontor system using 532 nm laser excitation with a laser power of 50 mW. XPS and UPS were performed using an NEXSA G2 (Thermo Scientific).

Testing of Odorant Sensing Performance. The chemiresistive response was measured using a custom-made odorant sensing test system. A combination of a system switch/multimeter (Keithley 3706A) and precision source/measure units (KEYSIGHT B2902A) was employed to measure the real-time electrical resistance of a multichannel sensor array. A DC voltage of 5 V was applied. An artificial olfactory chip with 10 integrated channels (20 mm × 20 mm) was mounted on a zig equipped with multiprobe tips for electrical probing. To control the measurement time for a single

https://doi.org/10.1021/acsnano.5c03601
ACS Nano 2025, 19, 17850−17862

channel at one point, the number of power line cycles (NPLC) was set to 1. Additionally, the delay time before and after moving to the next measurement was set to 0.001 s per point. Gas flow was controlled by a mass flow controller (M3030VA, Line Tech). All measurements were conducted at room temperature, with 10 min of exposure followed by 50 min of recovery. The concentration of odorant molecules was controlled by varying the ratio of base N_2 gas to carrier N_2 gas flowing into the odorant-containing bubbler. The total gas flow was maintained at 2000 sccm, with carrier gas:base gas ratios of 500:1500, 1000:1000, and 1500:500 to increase the concentration of odorant molecules. For mixed odorant experiments, we generated mixed odors by varying the carrier gas flow rates into two separate bubblers, each containing a different fragrance. The flow rate combinations were set to 500:1500, 1000:1000, and 1500:500 sccm, allowing us to create mixtures with varying ratios of concentration.

The response of the gas sensor was calculated using eq 1:

$$\text{Response} = (R - R_0)/R_0 \times 100\ (\%) \quad (1)$$

where R is the resistance after exposure of the target gas and R_0 is the initial resistance of the sensor.

Machine Learning-Based Data Processing. For data analysis, the response values of each sensor were used as features. The *t*-SNE analysis was performed to reduce the multidimensional parameters (Tables S4–S12) to 2D using the Python scikit-learn library. Classification of odorant types and regression for concentration prediction using SVM were performed with the Python scikit-learn library, utilizing an RBF kernel. The training set and test set were divided in a 7:3 ratio. Tanimoto coefficients for comparing molecular similarity were obtained by converting each chemical compound to a simplified molecular input line entry system (SMILES) notation and using the Python RDkit library.

Flexibility Test. The stress–strain (SS) curve and electrical resistance changes during the tensile process were measured using an SFM-100kN universal testing machine (United Calibration). The crosshead speed was 20 mm/min. Real-time resistance changes were recorded by connecting a jig and a digital multimeter (Keithley 2001) with a copper wire. For cyclic bending tests to evaluate fatigue failure, a 1-axis motion controller from SCIENCETOWN was utilized.

ASSOCIATED CONTENT

Supporting Information

The Supporting Information is available free of charge at https://pubs.acs.org/doi/10.1021/acsnano.5c03601.

Estimation of the energy band diagram of LIG; atomic percentages of carbon, oxygen, and cerium as a function of specific power and PPI; response data for D-limonene, 2,3,5-trimethylpyrazine, cis-3-hexenol, 2-ethyl-fenchol, geraniol, ethanol, eugenol, octanal, and heptanol; confusion matrix of the actual versus predicted classes in the test set; predicted odorant concentration versus true odorant concentration for 2,3,5-trimethylpyrazine, D-limonene, and 1-heptanol for the test set; molecular similarity calculation via Tanimoto coefficient; cyclic stress–strain curve showing stress softening (PDF)

AUTHOR INFORMATION

Corresponding Author

Hyuk-Jun Kwon − *Department of Electrical Engineering and Computer Science, DGIST, Daegu 42988, Republic of Korea; Convergence Research Advanced Centre for Olfaction, DGIST, Daegu 42988, Republic of Korea;* orcid.org/0000-0002-4767-7444; Email: hj.kwon@dgist.ac.kr

Authors

Hyeongtae Lim − *Department of Electrical Engineering and Computer Science, DGIST, Daegu 42988, Republic of Korea; Convergence Research Advanced Centre for Olfaction, DGIST, Daegu 42988, Republic of Korea;* orcid.org/0000-0001-6417-3312

Hyeokjin Kwon − *Department of Electrical Engineering and Computer Science, DGIST, Daegu 42988, Republic of Korea; Convergence Research Advanced Centre for Olfaction, DGIST, Daegu 42988, Republic of Korea*

Jae Eun Jang − *Department of Electrical Engineering and Computer Science, DGIST, Daegu 42988, Republic of Korea;* orcid.org/0000-0002-8523-1785

Complete contact information is available at: https://pubs.acs.org/10.1021/acsnano.5c03601

Author Contributions

H.L. and H.-J.K. conceived the concept. H.L. fabricated and characterized CeLIG e-nose. H.L. and H.K. conducted the gas-sensing experiments. H.L. and H.-J.K. conducted the flexibility test. H.L. wrote the paper. All the authors discussed the results and commented on the manuscript. H.-J.K. was responsible for managing all aspects of this project. All authors have given approval to the final version of the manuscript.

Funding

This work was supported by the National Research Foundation of Korea (NRF) funded by the Ministry of Science and ICT (MSIT) (RS-2024-00428887) and by the Ministry of Education (RS-2020-NR049577).

Notes

The authors declare no competing financial interest.

ACKNOWLEDGMENTS

This work was supported by the National Research Foundation of Korea (NRF) funded by the Ministry of Science and ICT (MSIT) (RS-2024-00428887) and by the Ministry of Education (RS-2020-NR049577).

REFERENCES

(1) Kim, C.; Lee, K. K.; Kang, M. S.; Shin, D.-M.; Oh, J.-W.; Lee, C.-S.; Han, D.-W. Artificial Olfactory Sensor Technology That Mimics the Olfactory Mechanism: A Comprehensive Review. *Biomater. Res.* **2022**, *26* (1), 40.

(2) Malnic, B.; Hirono, J.; Sato, T.; Buck, L. B. Combinatorial Receptor Codes for Odors. *Cell* **1999**, *96*, 713–723.

(3) Bushdid, C.; Magnasco, M. O.; Vosshall, L. B.; Keller, A. Humans Can Discriminate More Than 1 Trillion Olfactory Stimuli. *Science* **2014**, *343*, 1370–1372.

(4) Dinh, T.-V.; Choi, I.-Y.; Son, Y.-S.; Kim, J.-C. A Review on Non-Dispersive Infrared Gas Sensors: Improvement of Sensor Detection Limit and Interference Correction. *Sens. Actuators, B* **2016**, *231*, 529–538.

(5) Kumar, A.; Prajesh, R. The Potential of Acoustic Wave Devices for Gas Sensing Applications. *Sens. Actuators, A* **2022**, *339*, 113498.

(6) Dey, A. Semiconductor Metal Oxide Gas Sensors: A Review. *Mater. Sci. Eng., B* **2018**, *229*, 206–217.

(7) Nasri, A.; Boujnah, A.; Boubaker, A.; Kalboussi, A. A Smart Gas Sensor Using Machine Learning Algorithms: Sensor Types Based on IED Configurations, Fabrication Techniques, Algorithmic Approaches, Challenges, Progress, and Limitations: A Review. *IEEE Sens. J.* **2023**, *23*, 11336–11355.

(8) Lee, B.; Lee, J.; Lee, J.-O.; Hwang, Y.; Bahn, H.-K.; Park, I.; Jheon, S.; Lee, D.-S. Breath Analysis System with Convolutional

Neural Network (CNN) for Early Detection of Lung Cancer. *Sens. Actuators, B* **2024**, *409*, 135578.
(9) Jeong, S.- Y.; Kim, J.- S.; Lee, J.- H. Rational Design of Semiconductor-Based Chemiresistors and Their Libraries for Next-Generation Artificial Olfaction. *Adv. Mater.* **2020**, *32* (51), 2002075.
(10) Wang, C.; Chen, Z.; Chan, C. L. J.; Wan, Z. A.; Ye, W.; Tang, W.; Ma, Z.; Ren, B.; Zhang, D.; Song, Z.; Ding, Y.; Long, Z.; Poddar, S.; Zhang, W.; Wan, Z.; Xue, F.; Ma, S.; Zhou, Q.; Lu, G.; Liu, K. Biomimetic Olfactory Chips Based on Large-Scale Monolithically Integrated Nanotube Sensor Arrays. *Nat. Electron.* **2024**, *7*, 157−165.
(11) Moon, H. G.; Jung, Y.; Shin, B.; Song, Y. G.; Kim, J. H.; Lee, T.; Lee, S.; Jun, S. C.; Kaner, R. B.; Kang, C.-Y.; et al. On-Chip Chemiresistive Sensor Array for On-Road NO_x Monitoring with Quantification. *Adv. Sci.* **2020**, *7* (22), 2002014.
(12) Kang, H.; Cho, S.-Y.; Ryu, J.; Choi, J.; Ahn, H.; Joo, H.; Jung, H.-T. Multiarray Nanopattern Electronic Nose (E-Nose) by High-Resolution Top-Down Nanolithography. *Adv. Funct. Mater.* **2020**, *30* (27), 2002486.
(13) Henriquez, D. V. D. O.; Kang, M.; Cho, I.; Choi, J.; Park, J.; Gul, O.; Ahn, J.; Lee, D.- S.; Park, I. Multi-Transduction Nanosensor Array for Accurate Sensing of Flammable and Toxic Gases. *Small Methods* **2023**, *7* (3), 2201352.
(14) Jeong, S.-Y.; Moon, Y. K.; Wang, J.; Lee, J.-H. Exclusive Detection of Volatile Aromatic Hydrocarbons Using Bilayer Oxide Chemiresistors with Catalytic Overlayers. *Nat. Commun.* **2023**, *14* (1), 233.
(15) Goschnick, J.; Koronczi, I.; Frietsch, M.; Kiselev, I. Water Pollution Recognition with the Electronic Nose KAMINA. *Sens. Actuators, B* **2005**, *106*, 182−186.
(16) Alizadeh, T.; Soltani, L. H. Reduced Graphene Oxide-Based Gas Sensor Array for Pattern Recognition of DMMP Vapor. *Sens. Actuators, B* **2016**, *234*, 361−370.
(17) Liu, X.; He, Z.; Xu, S.; Wu, J.; Wu, J. Assembly of 2D-MoS_2 with Graphene Layer for Highly Sensitive and Selective Gas Detection at Room Temperature. *Sens. Actuators, B* **2022**, *367*, 132185.
(18) Liu, X.; Chen, Q.; Xu, S.; Wu, J.; Zhao, J.; He, Z.; Pan, A.; Wu, J. A Prototype of Graphene E-Nose for Exhaled Breath Detection and Label-Free Diagnosis of Helicobacter Pylori Infection. *Adv. Sci.* **2024**, *11*, 2401695.
(19) Le, T.- S. D.; Phan, H.- P.; Kwon, S.; Park, S.; Jung, Y.; Min, J.; Chun, B. J.; Yoon, H.; Ko, S. H.; Kim, S.- W.; Kim, Y. - J. Recent Advances in Laser-Induced Graphene: Mechanism, Fabrication, Properties, and Applications in Flexible Electronics. *Adv. Funct. Mater.* **2022**, *32* (48), 2205158.
(20) Lin, J.; Peng, Z.; Liu, Y.; Ruiz-Zepeda, F.; Ye, R.; Samuel, E. L.; Yacaman, M. J.; Yakobson, B. I.; Tour, J. M. Laser-Induced Porous Graphene Films from Commercial Polymers. *Nat. Commun.* **2014**, *5*, 5714.
(21) Vivaldi, F. M.; Dallinger, A.; Bonini, A.; Poma, N.; Sembranti, L.; Biagini, D.; Salvo, P.; Greco, F.; Di Francesco, F. D. (3D) Laser-Induced Graphene: Structure, Properties, and Application to Chemical Sensing. *ACS Appl. Mater. Interfaces* **2021**, *13* (26), 30245−30260.
(22) Yang, L.; Yan, J.; Meng, C.; Dutta, A.; Chen, X.; Xue, Y.; Niu, G.; Wang, Y.; Du, S.; Zhou, P.; Zhang, C.; Guo, S.; Cheng, H. Vanadium Oxide-Doped Laser-Induced Graphene Multi-Parameter Sensor to Decouple Soil Nitrogen Loss and Temperature. *Adv. Mater.* **2023**, *35* (14), 2210322.
(23) Lim, H.; Kwon, H.; Kang, H.; Jang, J. E.; Kwon, H.-J. Semiconducting MOFs on Ultraviolet Laser-Induced Graphene with a Hierarchical Pore Architecture for NO_2 Monitoring. *Nat. Commun.* **2023**, *14* (1), 3114.
(24) Yan, W.; Yan, W.; Chen, T.; Xu, J.; Tian, Q.; Ho, D. Size-Tunable Flowerlike MoS_2 Nanospheres Combined with Laser-Induced Graphene Electrodes for NO_2 Sensing. *ACS Appl. Nano Mater.* **2020**, *3*, 2545−2553.
(25) Nasser, J.; Lin, J.; Zhang, L.; Sodano, H. A. Laser Induced Graphene Printing of Spatially Controlled Super-Hydrophobic/Hydrophilic Surfaces. *Carbon* **2020**, *162*, 570−578.
(26) Duy, L. X.; Peng, Z.; Li, Y.; Zhang, J.; Ji, Y.; Tour, J. M. Laser-Induced Graphene Fibers. *Carbon* **2018**, *126*, 472−479.
(27) Abdulhafez, M.; Tomaraei, G. N.; Bedewy, M. Fluence-Dependent Morphological Transitions in Laser-Induced Graphene Electrodes on Polyimide Substrates for Flexible Devices. *ACS Appl. Nano Mater.* **2021**, *4*, 2973−2986.
(28) Montini, T.; Melchionna, M.; Monai, M.; Fornasiero, P. Fundamentals and Catalytic Applications of CeO_2-Based Materials. *Chem. Rev.* **2016**, *116*, 5987−6041.
(29) Baek, J. W.; Han, S.; Lee, S. E.; Ahn, J.; Park, C.; Nam, J. S.; Kim, Y. H.; Shin, E.; Kim, M.; Jang, J. S.; Kim, J.; Park, H. J.; Kim, I. D. Cobalt-Doped Ceria Sensitizer Effects on Metal Oxide Nanofibers: Heightened Surface Reactivity for High-Performing Chemiresistive Sensors. *ACS Nano* **2024**, *18*, 19568−19580.
(30) Hu, J.; Zou, C.; Su, Y.; Li, M.; Ye, X.; Cai, B.; Kong, E. S.-W.; Yang, Z.; Zhang, Y. Light-Assisted Recovery for a Highly-Sensitive NO_2 Sensor Based on RGO-CeO_2 Hybrids. *Sens. Actuators, B* **2018**, *270*, 119−129.
(31) Zhang, L.; Xu, H.; Huang, Y.; Lu, H.; Ai, T.; Xu, K.; Ma, F.; Chu, P. K. Polar Cubic CeO_2 Nanoparticles on Graphene for Enhanced Room-Temperature NO_2 Sensing Performance. *ACS Appl. Nano Mater.* **2023**, *6*, 10551−10558.
(32) Song, Z.; Ye, W.; Chen, Z.; Chen, Z.; Li, M.; Tang, W.; Wang, C.; Wan, Z.; Poddar, S.; Wen, X.; Pan, X.; Lin, Y.; Zhou, Q.; Fan, Z. Wireless Self-Powered High-Performance Integrated Nanostructured-Gas-Sensor Network for Future Smart Homes. *ACS Nano* **2021**, *15*, 7659−7667.
(33) Ye, R.; Peng, Z.; Wang, T.; Xu, Y.; Zhang, J.; Li, Y.; Nilewski, L. G.; Lin, J.; Tour, J. M. In Situ Formation of Metal Oxide Nanocrystals Embedded in Laser-Induced Graphene. *ACS Nano* **2015**, *9*, 9244−9251.
(34) Hui, X.; Xuan, X.; Kim, J.; Park, J. Y. A Highly Flexible and Selective Dopamine Sensor Based on Pt-Au Nanoparticle-Modified Laser-Induced Graphene. *Electrochim. Acta.* **2019**, *328*, 135066.
(35) Jeong, S.; Yang, S.; Lee, Y. J.; Lee, S. H. Laser-Induced Graphene Incorporated with Silver Nanoparticles Applied for Heavy Metal Multi-Detection. *J. Mater. Chem. A* **2023**, *11*, 13409−13418.
(36) Liu, Y.; Xue, Q.; Chang, C.; Wang, R.; Wang, Q.; Shan, X. Highly Efficient Detection of Cd(II) Ions by a Stannum and Cerium Bimetal-Modified Laser-Induced Graphene Electrode in Water. *Chem. Eng. J.* **2022**, *433*, 133791.
(37) Guo, S.; Zhao, Y.; Yuan, H.; Wang, C.; Jiang, H.; Cheng, G. J. Ultrafast Laser Manufacture of Stable, Efficient Ultrafine Noble Metal Catalysts Mediated with MOF Derived High Density Defective Metal Oxides. *Small* **2020**, *16* (18), 2000749.
(38) Zhang, Y.; Bals, S.; Van Tendeloo, G. Understanding CeO_2-Based Nanostructures Through Advanced Electron Microscopy in 2D and 3D. *Part Part Syst. Charact.* **2019**, *36* (1), 1800287.
(39) Kim, J. H.; Kim, J. K.; Liu, J.; Curcio, A.; Jang, J. S.; Kim, I. D.; Ciucci, F.; Jung, W. Nanoparticle Ex-Solution for Supported Catalysts: Materials Design, Mechanism and Future Perspectives. *ACS Nano* **2021**, *15*, 81−110.
(40) Thanh, N. T.; Maclean, N.; Mahiddine, S. Mechanisms of Nucleation and Growth of Nanoparticles in Solution. *Chem. Rev.* **2014**, *114*, 7610−7630.
(41) Kim, J. K.; Kim, S.; Kim, S.; Kim, H. J.; Kim, K.; Jung, W.; Han, J. W. Dynamic Surface Evolution of Metal Oxides for Autonomous Adaptation to Catalytic Reaction Environments. *Adv. Mater.* **2023**, *35* (4), 2203370.
(42) Khan, M. M.; Ansari, S. A.; Pradhan, D.; Han, D. H.; Lee, J.; Cho, M. H. Defect-Induced Band Gap Narrowed CeO_2 Nanostructures for Visible Light Activities. *Ind. Eng. Chem. Res.* **2014**, *53*, 9754−9763.
(43) Guo, Y.; Gong, M.; Li, Y.; Liu, Y.; Dou, X. Sensitive, Selective, and Fast Detection of ppb-Level H_2S Gas Boosted by ZnO-CuO Mesocrystal. *Nanoscale Res. Lett.* **2016**, *11* (1), 475.
(44) Wang, H.; Zhao, Z.; Liu, P.; Guo, X. A Soft and Stretchable Electronics Using Laser-Induced Graphene on Polyimide/PDMS Composite Substrate. *Npj Flexible Electron.* **2022**, *6* (1), 26.

https://doi.org/10.1021/acsnano.5c03601
ACS Nano 2025, 19, 17850−17862

(45) Beckham, J. L.; Li, J. T.; Stanford, M. G.; Chen, W.; McHugh, E. A.; Advincula, P. A.; Wyss, K. M.; Chyan, Y.; Boldman, W. L.; Rack, P. D.; Tour, J. M. High-Resolution Laser-Induced Graphene from Photoresist. *ACS Nano* **2021**, *15*, 8976−8983.
(46) Eckmann, A.; Felten, A.; Mishchenko, A.; Britnell, L.; Krupke, R.; Novoselov, K. S.; Casiraghi, C. Probing the Nature of Defects in Graphene by Raman Spectroscopy. *Nano Lett.* **2012**, *12*, 3925−3930.
(47) Yoon, J.-W.; Kim, J.-S.; Kim, T.-H.; Hong, Y. J.; Kang, Y. C.; Lee, J.-H. A New Strategy for Humidity Independent Oxide Chemiresistors: Dynamic Self-Refreshing of In_2O_3 Sensing Surface Assisted by Layer-by-Layer Coated CeO_2 Nanoclusters. *Small* **2016**, *12*, 4229−4240.
(48) Cheng, G.; Song, Z.; Mao, Y.; Zhang, J.; Wang, K.; Li, H.; Huang, Z. Effect of Ce_2O_3 Phase Transition on the Catalytic Oxidation for Toluene over CeO_2 Catalysts. *Fuel* **2024**, *368*, 131641.
(49) Shyu, J.; Weber, W.; Gandhi, H. Surface Characterization of Alumina-Supported Ceria. *J. Phys. Chem.* **1988**, *92*, 4964−4970.
(50) Preisler, E.; Marsh, O.; Beach, R.; McGill, T. Stability of Cerium Oxide on Silicon Studied by X-Ray Photoelectron Spectroscopy. *J. Vac. Sci. Technol. B* **2001**, *19*, 1611−1618.
(51) Palneedi, H.; Park, J. H.; Maurya, D.; Peddigari, M.; Hwang, G.−T.; Annapureddy, V.; Kim, J.−W.; Choi, J.−J.; Hahn, B.−D.; Priya, S.; Lee, K. J.; Ryu, J. Laser Irradiation of Metal Oxide Films and Nanostructures: Applications and Advances. *Adv. Mater.* **2018**, *30* (14), 1705148.
(52) Ma, R.; Islam, M. J.; Reddy, D. A.; Kim, T. K. Transformation of CeO_2 into a Mixed Phase CeO_2/Ce_2O_3 Nanohybrid by Liquid Phase Pulsed Laser Ablation for Enhanced Photocatalytic Activity Through Z-Scheme Pattern. *Ceram. Int.* **2016**, *42* (16), 18495−18502.
(53) Rastogi, S. C.; Heydorn, S.; Johansen, J. D.; Basketter, D. A. Fragrance Chemicals in Domestic and Occupational Products. *Contact Dermatitis* **2001**, *45*, 221−225.
(54) Van der Maaten, L.; Hinton, G. Visualizing Data Using t-SNE. *J. Mach. Learn. Res.* **2008**, *9*, 2579−2605.
(55) Müller, A. C.; Guido, S. *Introduction to Machine Learning with Python: A Guide for Data Scientists*; O'Reilly, 2016.
(56) Bajusz, D.; Rácz, A.; Héberger, K. Why Is Tanimoto Index an Appropriate Choice for Fingerprint-Based Similarity Calculations? *J. Cheminf.* **2015**, *7* (1), 20.
(57) Song, H. W.; Moon, D.; Won, Y.; Cha, Y. K.; Yoo, J.; Park, T. H.; Oh, J. H. A Pattern Recognition Artificial Olfactory System Based on Human Olfactory Receptors and Organic Synaptic Devices. *Sci. Adv.* **2024**, *10* (21), No. eadl2882.
(58) Khatib, M.; Rapoport, S.; Zohar, O.; Mansour, E.; Zheng, Y.; Tang, N.; Saliba, W.; Mulytin, Y.; Huynh, T.−P.; Haick, H. Hierarchical Graphene-Dye Bilayers for Multimodal Optoelectronic Sensing and Decoupling of Complex Stimuli. *Adv. Mater. Technol.* **2023**, *8* (3), 2200920.
(59) Alzate-Carvajal, N.; Park, J.; Bargaoui, I.; Rautela, R.; Comeau, Z. J.; Scarfe, L.; Ménard, J.-M.; Darling, S. B.; Lessard, B. H.; Luican-Mayer, A. Arrays of Functionalized Graphene Chemiresistors for Selective Sensing of Volatile Organic Compounds. *ACS Appl. Electron. Mater.* **2023**, *5*, 1514−1520.
(60) Tran, A. T. T.; Hassan, K.; Tung, T. T.; Tripathy, A.; Mondal, A.; Losic, D. Graphene and Metal-Organic Framework Hybrids for High-Performance Sensors for Lung Cancer Biomarker Detection Supported by Machine Learning Augmentation. *Nanoscale* **2024**, *16*, 9084−9095.
(61) Cho, I.; Lee, K.; Sim, Y. C.; Jeong, J.−S.; Cho, M.; Jung, H.; Kang, M.; Cho, Y.−H.; Ha, S. C.; Yoon, K.−J.; et al. Deep-Learning-Based Gas Identification by Time-Variant Illumination of a Single Micro-LED-Embedded Gas Sensor. *Light: Sci. Appl.* **2023**, *12* (1), 95.
(62) Wu, X.; Jiang, L.; Xu, H.; Wang, B.; Yang, L.; Wang, X.; Zheng, L.; Xu, W.; Qiu, L. Bionic Olfactory Synaptic Transistors for Artificial Neuromotor Pathway Construction and Gas Recognition. *Adv. Funct. Mater.* **2024**, *34* (36), 2401965.
(63) Ogbeide, O.; Bae, G.; Yu, W.; Morrin, E.; Song, Y.; Song, W.; Li, Y.; Su, B.−L.; An, K.−S.; Hasan, T. Inkjet-Printed rGO/Binary Metal Oxide Sensor for Predictive Gas Sensing in a Mixed Environment. *Adv. Funct. Mater.* **2022**, *32* (25), 2113348.
(64) Kwon, H.; Kamboj, O.; Song, A.; Alarcon-Correa, M.; Remke, J.; Moafian, F.; Miksch, B.; Goyal, R.; Kim, D. Y.; Hamprecht, F. A.; Fischer, P. Scalable Optical Nose Realized with a Chemiresistively Modulated Light-Emitter Array. *Adv. Mater.* **2024**, *36* (29), 2402287.
(65) Lee, K.; Cho, I.; Kang, M.; Jeong, J.; Choi, M.; Woo, K. Y.; Yoon, K.-J.; Cho, Y.-H.; Park, I. Ultra-Low-Power E-Nose System Based on Multi-Micro-LED-Integrated, Nanostructured Gas Sensors and Deep Learning. *ACS Nano* **2023**, *17*, 539−551.
(66) Chen, Z.; Wang, J.; Pan, D.; Wang, Y.; Noetzel, R.; Li, H.; Xie, P.; Pei, W.; Umar, A.; Jiang, L.; Li, N.; Rooij, N. F. D.; Zhou, G. Mimicking a Dog's Nose: Scrolling Graphene Nanosheets. *ACS Nano* **2018**, *12*, 2521−2530.
(67) Zhao, J.; Yi, N.; Ding, X.; Liu, S.; Zhu, J.; Castonguay, A. C.; Gao, Y.; Zarzar, L. D.; Cheng, H. In Situ Laser-Assisted Synthesis and Patterning of Graphene Foam Composites as a Flexible Gas Sensing Platform. *Chem. Eng. J.* **2023**, *456*, 140956.
(68) Chen, Z.; Guo, H.; Zhang, F.; Li, X.; Yu, J.; Chen, X. Porous ZnO/rGO Nanosheet-Based NO_2 Gas Sensor with High Sensitivity and ppb-Level Detection Limit at Room Temperature. *Adv. Mater. Interfaces* **2021**, *8* (24), 2101511.
(69) Cui, X.; Tian, X.; Xiao, X.; Chen, T.; Wang, Y. Au Modified Hollow Cube Sn-MOF Derivatives for Highly Sensitive, Great Selective, and Stable Detection of n-Butanol at Room Temperature. *Adv. Mater. Technol.* **2023**, *8* (18), 2300572.
(70) Ozer, E.; Kufel, J.; Myers, J.; Biggs, J.; Brown, G.; Rana, A.; Sou, A.; Ramsdale, C.; White, S. A Hardwired Machine Learning Processing Engine Fabricated with Submicron Metal-Oxide Thin-Film Transistors on a Flexible Substrate. *Nat. Electron.* **2020**, *3*, 419−425.
(71) Diani, J.; Fayolle, B.; Gilormini, P. A Review on the Mullins Effect. *Eur. Polym. J.* **2009**, *45*, 601−612.

https://doi.org/10.1021/acsnano.5c03601
ACS Nano 2025, 19, 17850−17862